HHS Public Access

Author manuscript

Mol Imaging Biol. Author manuscript; available in PMC 2015 July 08.

Published in final edited form as:

Mol Imaging Biol. 2014 February ; 16(1): 36–43. doi:10.1007/s11307-013-0671-6.

Magnetomotive Optical Coherence Tomography for the Assessment of Atherosclerotic Lesions Using $\alpha_v\beta_3$ Integrin-Targeted Microspheres

Jongsik Kim[1], **Adeel Ahmad**[2], **Marina Marjanovic**[1,3], **Eric J. Chaney**[1], **Joanne Li**[4], **Jonathan Rasio**[5], **Zita Hubler**[3], **Darold Spillman**[1], **Kenneth S. Suslick**[1,6], and **Stephen A. Boppart**[1,2,3,7]

[1]Beckman Institute for Advanced Science and Technology, University of Illinois at Urbana-Champaign, 405 North Mathews Avenue, Urbana, IL 61801, USA

[2]Department of Electrical and Computer Engineering, University of Illinois at Urbana-Champaign, 1406 West Green Street, Urbana, IL 61801, USA

[3]Department of Bioengineering, University of Illinois at Urbana-Champaign, 1304 West Springfield Avenue, Urbana, IL 61801, USA

[4]Department of Nuclear, Plasma and Radiological Engineering, University of Illinois at Urbana-Champaign, 104 South Wright Street, Urbana, IL 61801, USA

[5]Department of Biochemistry, University of Illinois at Urbana-Champaign, 600 South Mathews Avenue, Urbana, IL 61801, USA

[6]Department of Chemistry, University of Illinois at Urbana-Champaign, 505 South Mathews Avenue, Urbana, IL 61801, USA

[7]Department of Internal Medicine, University of Illinois at Urbana-Champaign, 506 South Mathews Avenue, Urbana, IL 61801, USA

Abstract

Purpose—We investigated the early-stage fatty streaks/plaques detection using magnetomotive optical coherence tomography (MM-OCT) in conjunction with $\alpha_v\beta_3$ integrin-targeted magnetic microspheres (MSs). The targeting of functionalized MSs was investigated by perfusing *ex vivo* aortas from an atherosclerotic rabbit model in a custom-designed flow chamber at physiologically relevant pulsatile flow rates and pressures.

Correspondence to: Stephen A. Boppart; boppart@illinois.edu.

Jongsik Kim and Adeel Ahmad both contributed equally to this work.

Electronic supplementary material The online version of this article (doi:10.1007/s11307-013-0671-6) contains supplementary material, which is available to authorized users.

Disclosures. All other authors declare that they have no conflict of interest except for Stephen A. Boppart who receives royalties from the Massachusetts Institute of Technology for patents related to optical coherence tomography.

Conference presentation. Ahmad A, Kim JS, Li J, *et al*. *Magnetomotive contrast in optical coherence tomography for detecting early-stage atherosclerosis using targeted microspheres*, Optical Society of America, Biomedical Optics (BIOMED), Miami, Florida, 29 April–2 May 2012.

Procedures—Aortas were extracted and placed in a flow chamber. Magnetic MS contrast agents were perfused through the aortas and MM-OCT, fluorescence confocal, and bright field microscopy were performed on the *ex vivo* aorta specimens for localizing the MSs.

Results—The results showed a statistically significant and stronger MM-OCT signal (3.30±1.73 dB) from the aorta segment perfused with targeted MSs, compared with the nontargeted MSs (1.18±0.94 dB) and control (0.78±0.41 dB) aortas. In addition, there was a good co-registration of MM-OCT signals with confocal microscopy.

Conclusions—Early-stage fatty streaks/plaques have been successfully detected using MM-OCT in conjunction with $\alpha_v\beta_3$ integrin-targeted magnetic MSs.

Keywords

Optical coherence tomography; Magnetomotive; Protein microspheres; Fatty streaks; Atherosclerosis; $\alpha_v\beta_3$ integrin; Flow chamber

Introduction

Optical coherence tomography (OCT) is rapidly emerging as a promising high-resolution medical and biological imaging modality to monitor many cardiovascular interventions and visualize cardiovascular disease [1–3], which is the leading cause of death in the USA [4]. This technique is attractive for medical imaging because it permits the imaging of tissue microstructure *in vivo*, yielding micron-scale resolution images without the need for tissue excision and histological processing [1–3].

Almost all clinical imaging modalities employ exogenous contrast agents to identify diseased sites and enhance diagnostic capabilities. OCT has also benefited from the use of contrast agents. A variety of contrast agents engineered to exploit their scattering or absorption properties have been developed for OCT [5–10]. Our group has been investigating the use of magnetic microspheres (MSs) as dynamic contrast agents for molecular-specific OCT imaging [5, 8, 11–13]. These MSs can be engineered to target specific cellular receptors and molecules while the oil core can incorporate magnetic nanoparticles (MNPs) to generate dynamic contrast using the magnetomotive (MM) principle [11–13]. MM-OCT contrast is generated through the perturbation of magnetic particles by an external magnetic field. These resulting displacements induce changes in the local scattering which alter the amplitude and phase of the OCT interference pattern and can be measured with nanoscale accuracy [11–13].

Standard intravascular OCT imaging is performed by incorporating fiber-optic imaging catheters within the OCT sample arm. This method has been extensively investigated for applications in cardiology [14–21]. Intravascular OCT is analogous to intravascular ultrasound, except reflections of near-infrared light are detected by the catheter, rather than sound. This fiber-optic catheter can be combined with other imaging modalities such as fluorescence, ultrasound, and photoacoustic imaging [22, 23].

The addition of contrast agents for use with intravascular OCT can enable site-specific molecular cardiovascular imaging, just as has been shown for ultrasound imaging using gas-

filled microbubbles [24]. Other research groups have demonstrated that externally injected particles can be taken up by macrophages in atherosclerotic plaques and can be detected by OCT [25, 26], however, in this study, we demonstrate contrast agents for OCT in cardiology that can target the specific biomarkers (e.g., $\alpha_v\beta_3$ integrin) overexpressed in atherosclerotic lesions. This is especially needed to enhance the early detection and localization of atherosclerotic lesions which may not be clearly evident in structural OCT imaging or in other imaging modalities. Therefore, the combination of intravascular OCT and targeted molecular contrast enhancement using a dynamic MM technique may potentially improve the sensitivity of early atherosclerotic lesion detection.

In this work, we fabricated arginine-glycine-aspartic acid (RGD)-functionalized protein MSs that target the $\alpha_v\beta_3$ integrin overexpressed in atherosclerotic lesions. These MSs were loaded with iron oxide MNPs and a fluorescence dye, enabling multimodal imaging using MM-OCT and fluorescence imaging. Using an atherosclerotic rabbit model, we demonstrate successful detection of early-stage fatty streaks/plaques using MM-OCT in conjunction with $\alpha_v\beta_3$ integrin-targeted magnetic MSs by perfusing *ex vivo* aortas in a custom-designed flow chamber.

Methods

Rabbit Diet and Tissue Preparation

Experiments were performed in compliance with an experimental protocol approved by the Institutional Animal Care and Use Committee at the University of Illinois at Urbana-Champaign. Four-month-old male New Zealand white rabbits (n=3; Myrtle's Rabbitry, Thompson's Station, TN) after an acclimation period of 1 week on standard chow diet (Teklad 2031 Global High-Fiber Rabbit Diet; Harlan, Indianapolis, IN) were transitioned to an atherogenic diet over 10 days by substituting 10 % daily increments of cholesterol-containing diet (5TZB; TestDiet, Richmond, IN) for the standard rabbit chow diet [27, 28]. This approach induced atherosclerotic disease with varied fatty streaks and plaque composition in rabbits within 8∼9 weeks. After killing the animals, the aortas were divided into three segments and placed in our custom-designed flow chamber.

Microsphere Synthesis and In Vitro Cell Binding Test

Figure 1 illustrates the structure of a magnetic MS. The MSs used for this study had a core-shell structure, where the core consisted of hydrophobic vegetable oil, fluorescent Nile red dye, and iron oxide nanoparticles and the shell was hydrophilic, made of bovine serum albumin (Fisher Scientific, Pittsburgh, PA) protein [5, 7, 13]. The preparation protocol for these MSs has been previously described (Supplemental Fig. 1) [5, 7, 13]. MS size measurements were performed using a Coulter Counter (Multisizer 4, Beckman Coulter, Inc., Brea, CA) to measure both the concentration and size distribution (1–5 μm) of the MSs (Fig. 1d).

Flow Chamber

To mimic *in vivo* pulsatile flow and pressure conditions, a custom-designed flow chamber was developed (Fig. 2). Each aorta segment was mounted between the plastic inlet and

outlet tubes inside the chamber. A pulsatile high-pressure blood pump (1405 Blood Pump, Harvard Apparatus, MA) designed to replicate the *in vivo* conditions in a rabbit was connected to the aortas to circulate the magnetic MSs through the aorta segment. A temperature sensor (6400K, OMEGA Engineering, Inc., CT) and pressure sensor (blood pressure transducer, Harvard Apparatus, MA) were continuously monitored while perfusing the aorta segments. Approximately, 10^9 MSs were added to 250 ml of phosphate-buffered saline (PBS; intraluminal fluid) which was contained in a temperature-controlled reservoir. The intraluminal fluid was perfused and circulated at a rate of 150 bpm using the pulsatile pump. The systolic and diastolic pressures were maintained at 150 and 70 mmHg, respectively, and the temperatures of the luminal and extraluminal fluid were maintained at 37 (±1)°C. Manganese (2 mM) was also added to the circulating intraluminal solution to enhance the affinity of integrin-binding sites for the RGD peptide on the early-stage fatty streaks and atherosclerotic plaques [29, 30]. Each aorta segment (n=3 per group; three groups) was perfused for 30 min with one of the following solutions in a randomized fashion: (1) RGD-functionalized MSs+PBS, (2) nonfunctionalized MSs+PBS, and (3) PBS only.

Tissue Imaging with MM-OCT and Fluorescent Confocal Microscopy

Each segment after 30 min of perfusion was cut open longitudinally, washed with fresh PBS three times, and placed on a microscope slide for MM-OCT imaging (Fig. 3) and fluorescence confocal imaging (TCS SP2 RBB, Leica Microsystems Inc., IL). The scans were performed in the periphery of branch vessel openings, as fatty streaks commonly develop around the openings, as well as other areas away from these openings. The MM-OCT system was based on a spectral-domain OCT system with the addition of a solenoid coil placed above the specimen in the sample arm as shown in Fig. 3. This OCT system, with a titanium/sapphire femtosecond laser (KMLabs, Inc., CO) as an optical source, produced 800 nm light with a bandwidth of 100 nm. The axial and transverse resolutions were ∼3 and 16 μm, respectively. The camera exposure time of the OCT system was 250 μs/A-line. An OCT B-mode image (2,048×4,000 pixels) was acquired with a line scan rate of 1,000 A-scans/s, giving a total acquisition time of 4 s. The optical imaging depth from the spectrometer was 2 mm, and the displacement sensitivity based on the phase noise of the system was approximately 11 nm. A detailed description of the MM-OCT processing method is available in the Electronic Supplementary Material (Supplemental Fig. 4). Briefly, a magnetic field strength of 400 Gauss with a driving frequency of 100 Hz was used to perturb any magnetic MSs in the specimens, and the changes in the magnitude and phase of the interference pattern were detected in synchrony with the scan rate and AC magnetic field modulation frequency to obtain the magnetic response from the specimens. The phase changes corresponding to the modulation frequency (100 Hz) were filtered out and the data were normalized with respect to an image captured with the magnetic field off to generate an MM-OCT image. The red and green channels (Supplemental Fig. 4c) represent the structural OCT signal and the MM signal due to the AC magnetic field, respectively. In addition, fluorescent confocal microscopy (Leica SP2 Visible Laser Confocal, Microscope, Leica Microsystems, IL) was performed on the same sites where MM-OCT images were acquired to further validate the presence of MSs by the detection of the fluorescent Nile red dye contained within the core of the MSs.

Histological Analysis

Histological features of fatty streaks and plaques were identified using hematoxylin and eosin (H&E) and Oil Red O (solvent red 27) staining. One half of the tissue cryo-sections (7 μm thickness) corresponding to the MM-OCT scan locations were stained with H&E while the other half of the cryo-sections were stained with Oil Red O, which stains lipids (i.e., fat) and neutral triglycerides.

Statistical Analysis

The correlation between groups: control vs. nontargeted MSs, control vs. targeted MSs, and nontargeted MSs vs. targeted MSs, was investigated by analysis of variance (95 % confidence interval) statistics followed by pairwise comparisons with post hoc Bonferroni correction (R software ver. 2.15.0). All values are given as mean±standard deviation.

Results

Figure 4 shows representative aorta specimens with early-stage fatty streaks and plaques. Oil red O staining (Fig. 4b) of the tissue cross sections labeled by the yellow dotted line on Fig. 4a revealed the presence of a lipid core. Based on the visual appearance of the aorta (Fig. 5a–c) and histological sections (Fig. 5d–f), early-stage fatty streaks and lipid-filled plaques were clearly visible. Figure 5d–f (H&E-stained tissue cross sections) shows a thickened intima and fibrous cap, typical of an atherosclerotic lesion.

To determine whether the $\alpha_v\beta_3$ integrin-targeted MSs were localized to early-stage fatty streaks, we performed MM-OCT imaging and fluorescence confocal microscopy at various locations (i.e., ≥3 locations per segment). Figure 5g–o shows representative MM-OCT images from the *ex vivo* aorta specimens. The green and red channels (Fig. 5m–o) represent the MM-OCT signal and structural OCT intensity, respectively.

The results in Table 1 and Fig. 6 show that there was a significantly stronger MM-OCT signal (3.30±1.73 dB) localized over the early-stage fatty streaks from the aorta segment perfused with targeted MSs, compared with the early-stage fatty streaks and plaques imaged in the nontargeted MSs (1.18±0.94 dB) and control (0.78±0.41 dB) aortas. The MM-OCT signal in the targeted MSs group was statistically significant and higher (p<0.001) than the MM-OCT signal in the nontargeted and control groups.

In addition, the same MM-OCT scan locations were imaged with fluorescence confocal microscopy (Supplemental Fig. 5) with an argon-ion laser at 488 nm as the excitation source and a ×10 objective lens. Even though MM-OCT and confocal images are at different planes (cross-sectional vs. *en face*, respectively) and have different resolutions and contrast mechanisms, they were obtained at the same locations to provide complementary information and validate the MM-OCT results. The fluorescence confocal images were in good agreement with the MM-OCT findings where the MM-OCT signal correlated (R^2 value= 0.9983; Supplemental Fig. 3) with the presence of localized MSs in the confocal images.

Discussion and Conclusion

In this study, we demonstrated the successful detection of early-stage atherosclerotic lesions using MM-OCT in conjunction with RGD-conjugated magnetic MSs. *Ex vivo* aorta specimens from a high-fat diet rabbit model were perfused in a custom-designed flow chamber at physiologically-relevant pulsatile flow rates and pressures. MM-OCT images from the $\alpha_v\beta_3$ integrin-targeted MS group clearly exhibit the localization of magnetic MSs to discrete lesions on the diseased intraluminal surface (i.e., fatty streaks). The results of fluorescence confocal microscopy and histological staining (i.e., H&E and Oil red O staining) further validate the MM-OCT findings.

Our previous study [6] demonstrated that these MSs can generate contrast in ultrasound imaging and the MNPs within the core can produce negative-T2 contrast in MRI. These MSs may be able to generate contrast in nuclear imaging (SPECT/PET) by incorporating radiotracers into the core or the shell as well. Moreover, these MSs were designed to be larger, blood-pool agents because they may also be loaded with drugs for targeted drug delivery applications [31]. We have also demonstrated that lipophilic fluorescence dyes can be incorporated within the core of these MSs, enabling these to be used for fluorescence imaging as well [5–7, 32]. In addition to generating contrast, MM-OCT can also be used to measure the biomechanical properties (i.e., elasticity) of the specimen microenvironment by exciting the MNPs or magnetic MSs with an external magnetic field [33, 34]. The biomechanical properties are highly correlated with disease progression and tissue characteristics in atherosclerotic plaque and cancer [35–37].

A low level of MM signal was seen in the MM-OCT images (Fig. 5k) from the nontargeted MS group. This result is due to the low level of nonspecific binding with nontargeted MSs as shown by our cell binding test results (Supplemental Fig. 2). Figure 5m shows that MM-OCT signal is visible deeper in the intimal and medial regions of the aorta specimen. The penetration of magnetic MSs into the deeper layers of tissue is highly unlikely because the average diameter of the MSs is around 3 μm. Particles of this size cannot readily pass through the endothelium, which acts as a semi-selective barrier between the blood vessel lumen and surrounding tissue. The MM signal observed from the deeper layers is therefore an artifact due to phase changes caused by the oscillating MSs at the more superficial layers, impacting the imaging at the deeper layers. These phase changes at the deeper layers may be due to the mechanical coupling between the targeted magnetic MSs, the intraluminal surface, and the deeper layers, or may be due to the bulk motion induced by the oscillating MSs. Similar artifacts have been observed in other phase-resolved methods such as Doppler OCT [38]. In other words, the MM-OCT imaging algorithm detects the tissue displacement induced by the oscillations of the targeted magnetic MSs, which is driven by the external AC magnetic field.

Several challenges were encountered during the flow chamber experiments including a decrease of MS concentration during flow. During tissue preparation, the side branch vessels were cut and the branch openings were subsequently closed by electrocautery (Bovie Medical Corporation, FL) before perfusing the aorta with intraluminal fluid (i.e., PBS+Mn +MSs). However, during the course of the experiments, some intraluminal fluid leaked

through the branch openings, resulting in a loss of intraluminal fluid volume and suspended MSs. To compensate for this loss, the circulating volume of the intraluminal fluid was maintained at a constant level by pumping some of the extraluminal fluid into the intraluminal fluid reservoir. However, this did not significantly dilute the concentration of the MSs in the intraluminal fluid.

In summary, we have shown that early-stage fatty streaks and plaques were successfully detected with targeted magnetic MSs using MM-OCT. Our future work involves the development of a novel solenoid configuration that can be incorporated with current commercial intravascular OCT systems, potentially enabling *in vivo* MM-OCT imaging. Further studies are also underway to understand the biodistribution and clearance of these MSs.

Supplementary Material

Refer to Web version on PubMed Central for supplementary material.

Acknowledgments

This research was supported in part by grants from the National Institutes of Health (NIBIB R01 EB009073) and a sponsored research agreement with Samsung, Inc. Jongsik Kim was funded by a Carle Foundation Hospital-Beckman Institute fellowship. Adeel Ahmad was funded at the University of Illinois by the NIH National Cancer Institute Alliance for Nanotechnology in Cancer (Midwest Cancer Nanotechnology Training Center) Grant R25-CA154015A.

References

1. Huang D, Swanson EA, Lin CP, et al. Optical coherence tomography. Science. 1991; 254:1178–1181. [PubMed: 1957169]
2. Tearney GJ, Waxman S, Shishkov M, et al. Three-dimensional coronary artery microscopy by intracoronary optical frequency domain imaging. JACC Cardiovasc Imaging. 2008; 1:752–761. [PubMed: 19356512]
3. Jones MR, Attizzani GF, Given CA 2nd, Brooks WH, Costa MA, Bezerra HG. Intravascular frequency-domain optical coherence tomography assessment of atherosclerosis and stent-vessel interactions in human carotid arteries. AJNR Am J Neuroradiol. 2012; 33:1494–1501. [PubMed: 22422179]
4. Farooq MU, Khasnis A, Majid A, Kassab MY. The role of optical coherence tomography in vascular medicine. Vasc Med. 2009; 14:63–71. [PubMed: 19144781]
5. Boppart SA, Oldenburg AL, Xu C, Marks DL. Optical probes and techniques for molecular contrast enhancement in coherence imaging. J Biomed Opt. 2005; 10:41208. [PubMed: 16178632]
6. John R, Rezaeipoor R, Adie SG, et al. *In vivo* magnetomotive optical molecular imaging using targeted magnetic nanoprobes. Proc Natl Acad Sci U S A. 2010; 107:8085–8090. [PubMed: 20404194]
7. John R, Nguyen FT, Kolbeck KJ, et al. Targeted multifunctional multimodal protein-shell microspheres as cancer imaging contrast agents. Mol Imaging Biol. 2012; 14:17–24. [PubMed: 21298354]
8. Lee TM, Oldenburg AL, Sitafalwalla S, et al. Engineered microsphere contrast agents for optical coherence tomography. Opt Lett. 2003; 28:1546–1548. [PubMed: 12956374]
9. Au KM, Lu Z, Matcher SJ, Armes SP. Polypyrrole nanoparticles: a potential optical coherence tomography contrast agent for cancer imaging. Adv Mater. 2011; 23:5792–5795. [PubMed: 22102372]

10. Jefferson A, Wijesurendra RS, McAteer MA, et al. Molecular imaging with optical coherence tomography using ligand-conjugated microparticles that detect activated endothelial cells: rational design through target quantification. Atherosclerosis. 2011; 219:579–587. [PubMed: 21872249]
11. Oldenburg AL, Toublan FJJ, Suslick KS, Wei A, Boppart SA. Magnetomotive contrast for *in vivo* optical coherence tomography. Opt Express. 2005; 13:6597–6614. [PubMed: 19498675]
12. Oldenburg AL, Crecea V, Rinne SA, Boppart SA. Phase-resolved magnetomotive OCT for imaging nanomolar concentrations of magnetic nanoparticles in tissues. Opt Express. 2008; 16:11525–11539. [PubMed: 18648474]
13. Toublan FJ, Boppart SA, Suslick KS. Tumor targeting by surface-modified protein microspheres. J Am Chem Soc. 2006; 128:3472–3473. [PubMed: 16536492]
14. Regar, E.; Leeuwen, TGV.; Serruys, PW. Optical Coherence Tomography in Cardiovascular Research. Informa Healthcare; Oxon, UK: 2007. p. 267-280.
15. Tearney GJ, Boppart SA, Bouma BE, et al. Scanning single-mode fiber optic catheter-endoscope for optical coherence tomography. Opt Lett. 1996; 21:543–545. [PubMed: 19865466]
16. Tearney GJ, Brezinski ME, Bouma BE, et al. *In vivo* endoscopic optical biopsy with optical coherence tomography. Science. 1997; 276:2037–2039. [PubMed: 9197265]
17. Nadkarni SK, Bouma BE, de Boer J, Tearney GJ. Evaluation of collagen in atherosclerotic plaques: the use of two coherent laser-based imaging methods. Lasers Med Sci. 2009; 24:439–445. [PubMed: 18386093]
18. Suter MJ, Nadkarni SK, Weisz G, et al. Intravascular optical imaging technology for investigating the coronary artery. JACC Cardiovasc Imaging. 2011; 4:1022–1039. [PubMed: 21920342]
19. Yoo H, Kim JW, Shishkov M, et al. Intra-arterial catheter for simultaneous microstructural and molecular imaging *in vivo*. Nat Med. 2011; 17:1680–1684. [PubMed: 22057345]
20. Wang Z, Chamie D, Bezerra HG, et al. Volumetric quantification of fibrous caps using intravascular optical coherence tomography. Biomed Opt Express. 2012; 3:1413–1426. [PubMed: 22741086]
21. Ayers JA, Tang WC, Chen Z. 360° rotating micro mirror for transmitting and sensing optical coherence tomography signals. Proc IEEE Sensors. 2004; 1:497–500.
22. Liang S, Saidi A, Jing J, et al. Intravascular atherosclerotic imaging with combined fluorescence and optical coherence tomography probe based on a double-clad fiber combiner. J Biomed Opt. 2012; 17:070501. [PubMed: 22894457]
23. Yang Y, Li X, Wang T, et al. Integrated optical coherence tomography, ultrasound and photoacoustic imaging for ovarian tissue characterization. Biomed Opt Express. 2011; 2:2551–2561. [PubMed: 21991547]
24. Peng S, Xiong Y, Li K, et al. Clinical utility of a microbubble-enhancing contrast (“SonoVue”) in treatment of uterine fibroids with high intensity focused ultrasound: a retrospective study. Eur J Radiol. 2012; 81:3832–3838. [PubMed: 22613505]
25. Paranjape AS, Kuranov R, Baranov S, et al. Depth resolved photothermal OCT detection of macrophages in tissue using nanorose. Biomed Opt Express. 2010; 1:2–16. [PubMed: 21258441]
26. Oh J, Feldman MD, Kim J, et al. Detection of macrophages in atherosclerotic tissue using magnetic nanoparticles and differential phase optical coherence tomography. J Biomed Opt. 2008; 13:054006. [PubMed: 19021386]
27. King JL, Miller RJ, Blue JP Jr, O'Brien WD Jr, Erdman JW Jr. Inadequate dietary magnesium intake increases atherosclerotic plaque development in rabbits. Nutr Res. 2009; 29:343–349. [PubMed: 19555816]
28. Smith BW, Simpson DG, Sarwate S, et al. Contrast ultrasound imaging of the aorta alters vascular morphology and circulating von Willebrand factor in hypercholesterolemic rabbits. J Ultrasound Med. 2012; 31:711–720. [PubMed: 22535718]
29. Bazzoni G, Ma L, Blue ML, Hemler ME. Divalent cations and ligands induce conformational changes that are highly divergent among beta1 integrins. J Biol Chem. 1998; 273:6670–6678. [PubMed: 9506964]
30. Dormond O, Ponsonnet L, Hasmim M, Foletti A, Rüegg C. Manganese-induced integrin affinity maturation promotes recruitment of alpha V beta 3 integrin to focal adhesions in endothelial cells:

evidence for a role of phosphatidylinositol 3-kinase and Src. Thromb Haemost. 2004; 92:151–161. [PubMed: 15213856]

31. Grinberg O, Hayun M, Sredni B, Gedanken A. Characterization and activity of sonochemically-prepared BSA microspheres containing Taxol–an anticancer drug. Ultrason Sonochem. 2007; 14:661–666. [PubMed: 17208504]
32. Olson ES, Whitney MA, Friedman B, et al. *In vivo* fluorescence imaging of atherosclerotic plaques with activatable cell-penetrating peptides targeting thrombin activity. Integr Biol (Camb). 2012; 4:595–605. [PubMed: 22534729]
33. Crecea V, Oldenburg AL, Liang X, Ralston TS, Boppart SA. Magnetomotive nanoparticle transducers for optical rheology of viscoelastic materials. Opt Express. 2009; 17:23114–23122. [PubMed: 20052238]
34. Oldenburg AL, Boppart SA. Resonant acoustic spectroscopy of soft tissues using embedded magnetomotive nanotransducers and optical coherence tomography. Phys Med Biol. 2010; 55:1189–1201. [PubMed: 20124653]
35. Koniari I, Mavrilas D, Papadaki H, et al. Structural and biomechanical alterations in rabbit thoracic aortas are associated with the progression of atherosclerosis. Lipids Health Dis. 2011; 10:125. [PubMed: 21791107]
36. Săftoiu A, Vilmann P, Hassan H, Gorunescu F. Analysis of endoscopic ultrasound elastography used for characterisation and differentiation of benign and malignant lymph nodes. Ultraschall Med. 2006; 27:535–542. [PubMed: 17160759]
37. Plewes DB, Bishop J, Samani A, Sciarretta J. Visualization and quantification of breast cancer biomechanical properties with magnetic resonance elastography. Phys Med Biol. 2000; 45:1591–1610. [PubMed: 10870713]
38. Yang VXD, Gordon ML, Mok A, et al. Improved phase-resolved optical Doppler tomography using the Kasai velocity estimator and histogram segmentation. Opt Commun. 2002; 208:209–214.

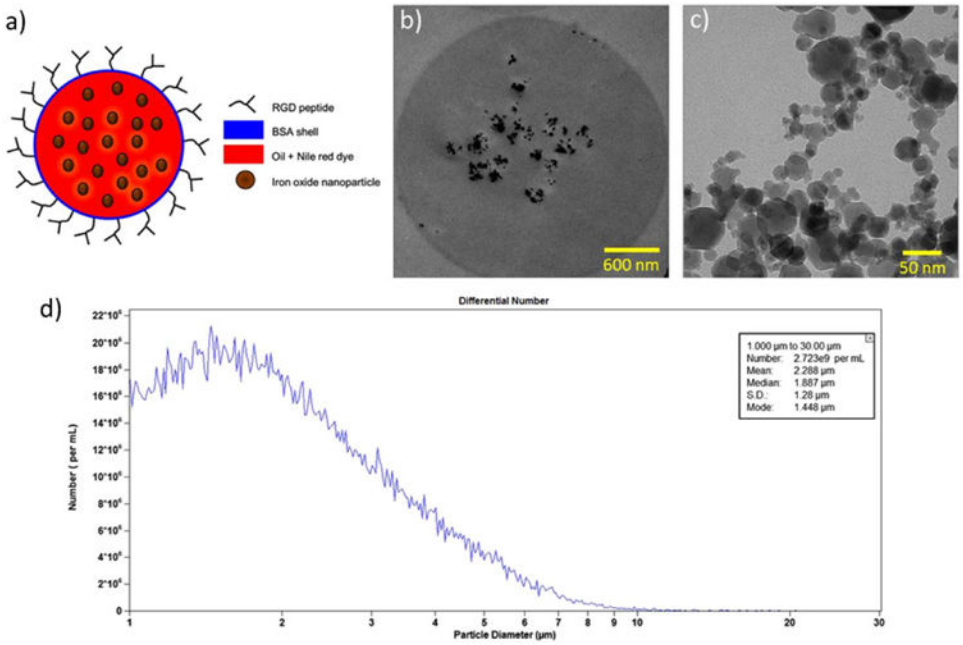

Fig 1.

Structure of the magnetic MSs: **a** conceptual drawing of the MS structure, **b** transmission electron microscopy (TEM) image of a single MS showing the presence of iron oxide nanoparticles and aggregates in the oil core, **c** TEM image of iron oxide nanoparticles and aggregates, and **d** a representative Coulter counter plot showing the size distribution of MSs.

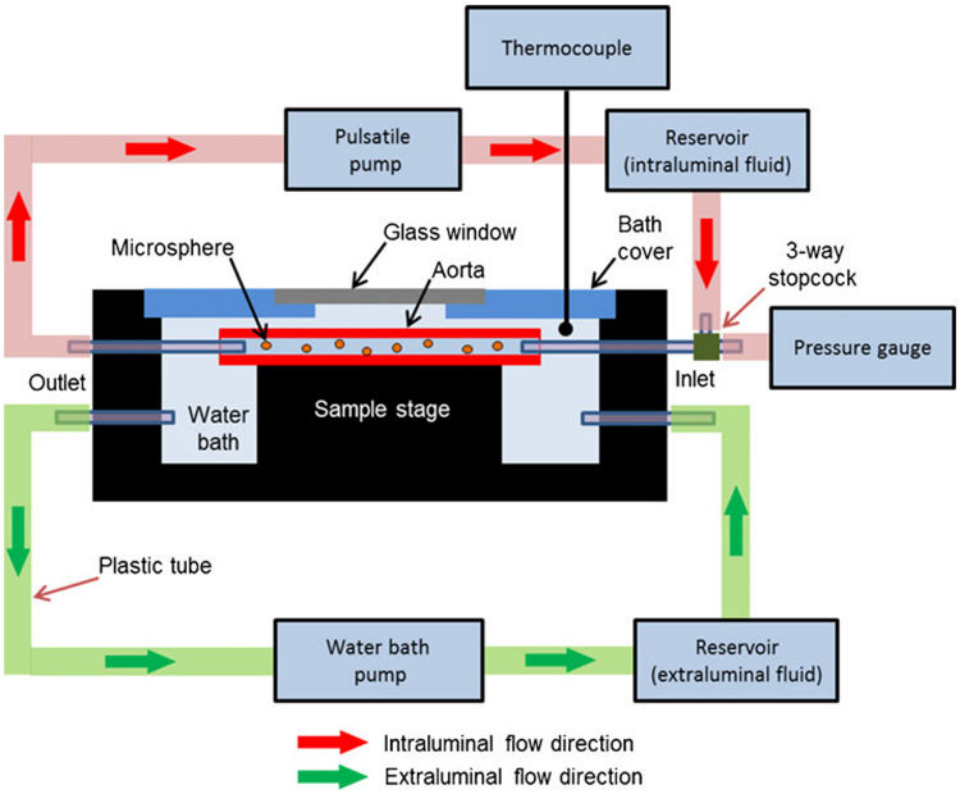

Fig 2.

Schematic of a custom-built flow chamber used for perfusing *ex vivo* aorta segments. The flow chamber consisted of a Plexiglas water bath container for extraluminal fluid (PBS). Each aorta segment was mounted between the plastic inlet and outlet tubes inside the chamber, whereas a pulsatile high-pressure blood pump was designed to replicate the *in vivo* conditions in a rabbit.

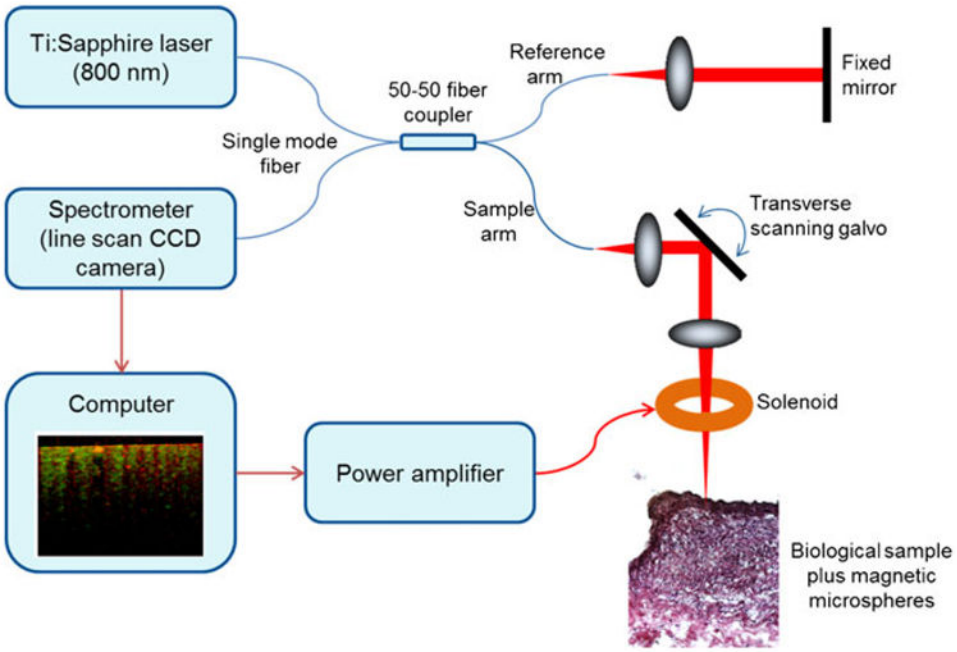

Fig 3.
Schematic of the MM-OCT system.

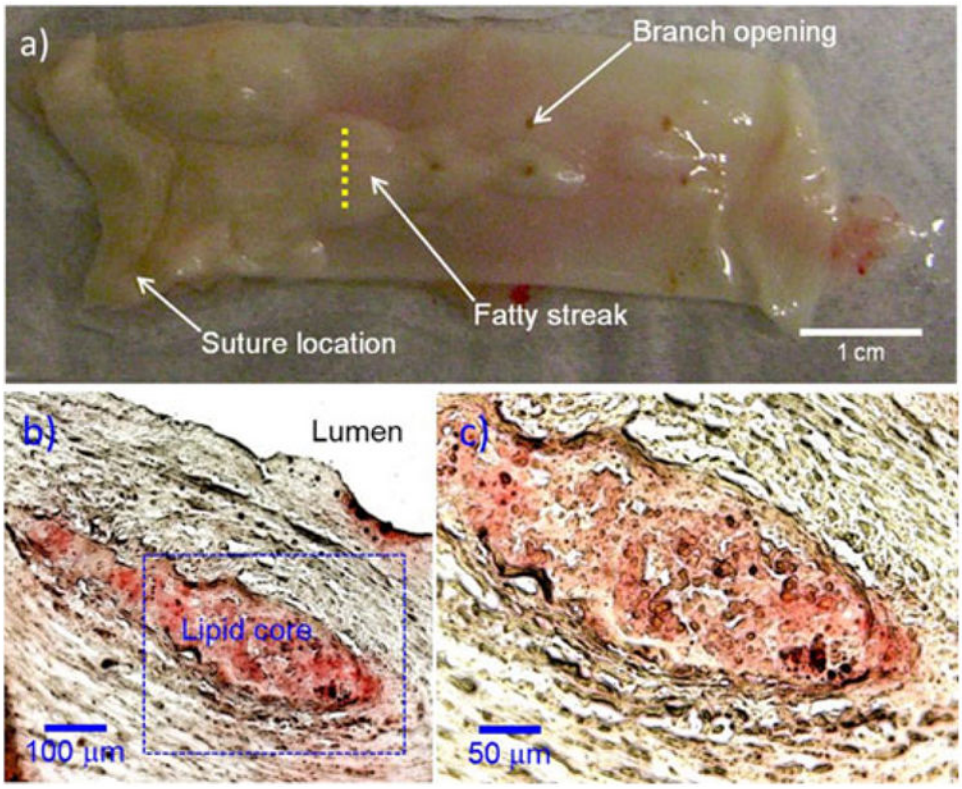

Fig 4.

Representative aorta specimen from a hyperlipidemic rabbit: **a** photograph of inner luminal wall, **b** Oil-red O-stained tissue cross section, **c** magnified image of the dotted *blue box* in (**b**). Histological Oil-red O stains the lipid core. The histological staining (**b**, **c**) along the *yellow dashed line* (**a**) reveals the presence of atherosclerotic plaque with lipid core.

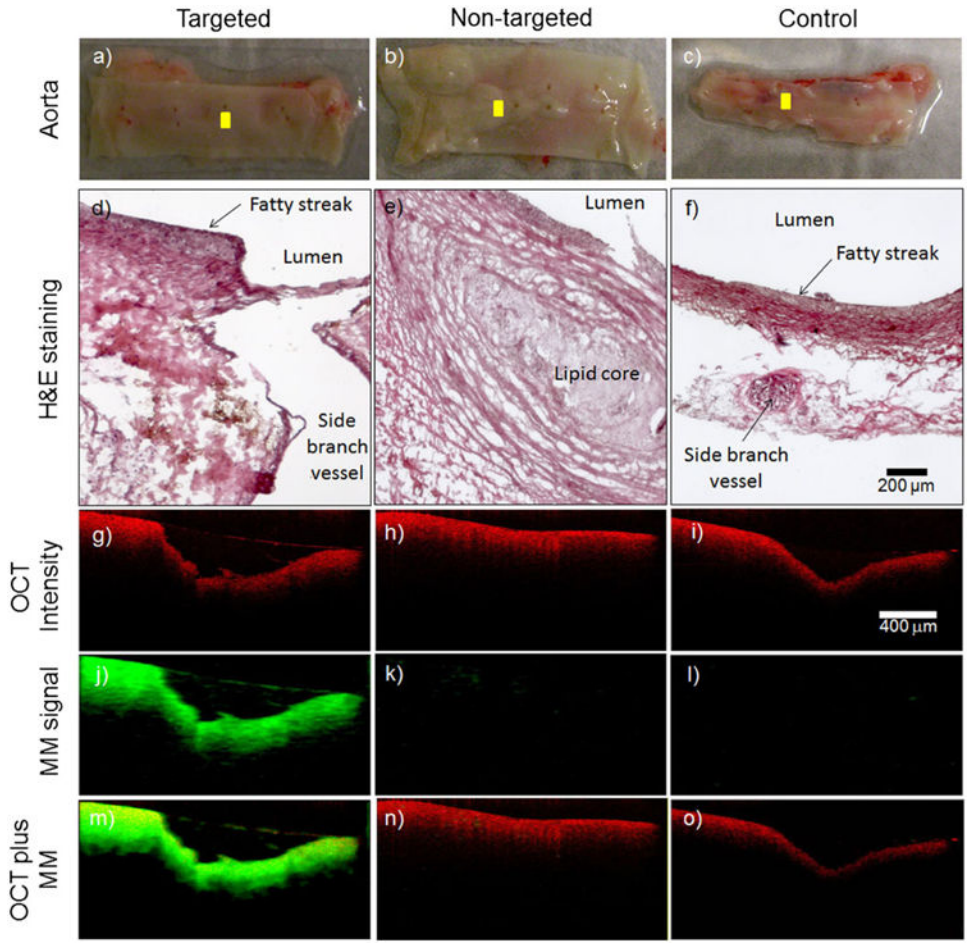

Fig 5.

Representative MM-OCT images from the *ex vivo* aorta specimens. The visual appearance of the luminal walls of the aortas (**a–c**) and corresponding histological sections (**d–f**) reveal the development of early-stage fatty streaks and plaques with lipid cores. OCT structural images (**g–i**) were superimposed (**m–o**) with MM images (**j–l**). The cross-sectional MM-OCT images correspond to the *yellow scan lines* shown in (**a–c**). The red and green channels represent the structural OCT intensity and MM-OCT signal, respectively.

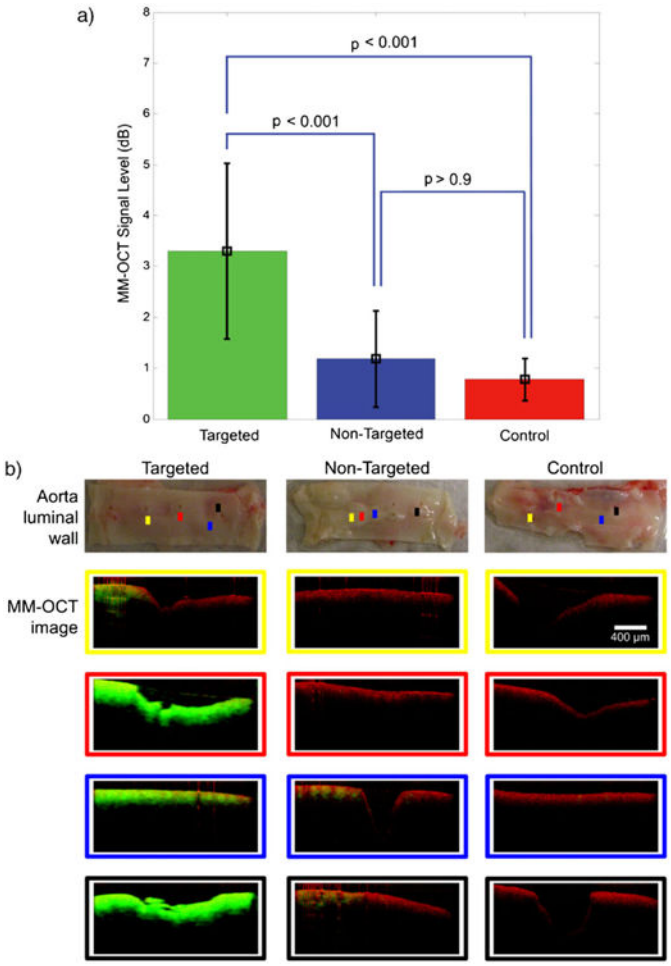

Fig 6.

Statistical comparison of MM-OCT signal between groups (**a**). The MM-OCT signal in the targeted MSs group was statistically significant and higher ($p<0.001$) than the nontargeted and control groups. There was no significant difference ($p>0.9$) between nontargeted and control groups. The *colored scan lines* in the aorta photos in (**b**) correspond to the MM-OCT scan locations. The scan images at these locations are identified with *color-matching boxes*. The *scale bar* (400 μm) applies to all the MM-OCT images. The *red* and *green channels* represent the structural OCT intensity and MM-OCT signal, respectively.

Table 1

Measured magnetomotive signal for targeted, nontargeted, and control groups

Group	No. of scan locations	Mean (±SD) of MM signal (dB)
Targeted (*n*=3)	19	3.30±1.73[a]
Nontargeted (*n*=3)	15	1.18±0.94[a]
Control (*n*=3)	10	0.78±0.41[a]

[a]Reported mean (±SD) values were obtained from the total number of scan locations within a group